Surface phonon polaritons on anisotropic piezoelectric superlattices

Yuanxi Chao, Jiteng Sheng, Jonathon A. Sedlacek, and James P. Shaffer
Homer L. Dodge Department of Physics and Astronomy, The University of Oklahoma, 440 W. Brooks Street, Norman, Oklahoma 73019, USA
(Received 5 October 2015; revised manuscript received 11 December 2015; published 19 January 2016)

A theoretical study of surface phonon polaritons (SPhPs) on periodically poled lithium niobate and periodically poled lithium tantalate surfaces is presented. We calculate the dielectric response for six different superlattice orientations and the associated SPhP dispersion relations. Our study of SPhPs accounts for the anisotropic nature of the dielectric response of the semi-infinite piezoelectric superlattices. We find that two different types of SPhPs can be supported. The first type consists of real surface dipole oscillations coupled to photons. The second type consists of virtual surface dipole oscillations driven by the incident photons. The dependence of the SPhPs on temperature and superlattice geometry is addressed. The use of these metamaterial excitations is discussed in the context of hybrid quantum systems.

DOI: 10.1103/PhysRevB.93.045419

I. INTRODUCTION

Surface polaritons have been studied for applications in subwavelength and near-field optical devices, energy transfer, and quantum hybrid systems [1–8]. The confined electromagnetic wave formed at the interface of two media by coupling photons to elementary excitations to create polaritons can be used for information transport. Most of the work on surface polaritons has been discussed from the perspective of surface plasmon polaritons (SPPs) [9]. SPPs are formed by coupling photons to surface charges, generally on metal surfaces. Recent research on surface phonon polaritons (SPhPs), where photons couple to optical phonons on dielectric surfaces, has been investigated for similar applications, usually in the infrared regime [10–17]. Similar to SPPs, SPhPs are interesting for future quantum information processing applications as a way to transport quantum information from a low to a high temperature environment [18] and, more fundamentally, the quantum control of mechanical vibrations. The coupling of electromagnetic waves to phonons and the propagation of SPhPs along a surface can be controlled by designing and engineering the material properties. In the case considered in this paper, we analyze superlattices engineered to have low frequency phonon modes that support SPhPs which can resonantly couple to highly excited atoms, such as Rydberg atoms.

For SPhPs on natural crystal surfaces, such as α-quartz, the polariton resonant frequencies are generally on the order of terahertz [19–21] and are difficult to tune. A piezoelectric superlattice (PSL) is a metamaterial with oppositely poled adjacent domains of a piezoelectric crystal [22,23]. A PSL has been shown to act as an artificial ionic-type phononic crystal [24]. With this picture, the superlattice domains can be viewed as periodically inverted dipoles whose oscillation produces phonons, and vice versa, due to the electromechanical coupling of the piezoelectric effect. Analogous to the dielectric response determined by the macroscopic equations of polar motion of an ionic crystal [25], the dielectric response of a PSL modified by the induced long-wavelength lattice waves can be calculated using piezoelectric equations [26]. This is an essential step for determining the characteristics of SPhPs on a PSL [27].

Among the many piezoelectric materials that we examined, periodically poled lithium niobate (PPLN) [28] and lithium tantalate (PPLT), which have been extensively studied for nonlinear optics, are promising PSLs for the study of SPhPs formed by electromechanical coupling. Both lithium niobate and lithium tantalate are classified as members of the $3m$ point group. They possess large piezoelectric coefficients with relatively small constant strain permittivity [29]. These qualities are desired for strong phonon-photon coupling.

It has been shown that the resonant frequencies of the lattice waves inside a PSL depend on its superlattice constant, which is the poling period of a periodically poled crystal [30]. SPhPs exist near some of these resonances [24,31]. As a result, using PPLN or PPLT with proper periodic poling can place the frequencies of SPhPs at the frequencies of specific transitions of Rydberg atoms, opening up the possibility to study the resonant atom-surface interaction in an experimentally more accessible regime. The atom-surface interaction can form an optomechanical hybrid quantum system where the atomic dipoles strongly couple to the surface guided electromechanical excitations in the near field regime, on the order of millimeters to meters.

Based on previous studies of SPhPs on PPLN and PPLT surfaces [26,31,32], we adopt and extend the method proposed in Ref. [33] to obtain the dielectric response of PPLN and PPLT. We further include the anisotropy of the dielectric response in our SPhP analysis [27,34]. We consider a PSL surface lying in the i-k plane, as shown in Fig. 1, with a superlattice-surface orientation of $T_i N_j$. T_i represents the superlattice direction lying parallel to the surface and normal to the lattice planes, $\hat{\imath}$, while N_j indicates the surface normal, $\hat{\jmath}$. The propagation direction of the induced lattice waves, due to the domain vibration, is always along $\hat{\imath}$.

The anisotropy of the PPLN and PPLT surfaces originates from the $3m$ single crystal structure [35,36] and the superlattice-surface orientations. Crystal structure can have a large effect on the way an electromagnetic wave propagates in and on the surface of a material [37]. The crystal structure of the lithium niobate and lithium tantalate used to construct the PSL is $3m$. The one-dimensional (1D) structure of the PSL breaks the $3m$ symmetry. A $3m$ crystal structure results in a uniaxial PSL for some geometries. Certain superlattice-surface arrangements, $T_x N_y$, $T_x N_z$, $T_y N_x$, and $T_y N_z$, result in a biaxial PSL. Both the 1D structure of the PSL and the symmetry of

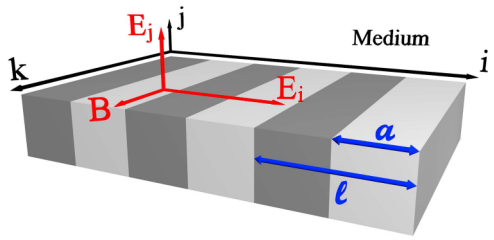

FIG. 1. Schematic sketch of a T_iN_j orientated PSL surface for a TM-mode SPhP. The interface is formed between the PSL and an isotropic medium. We define a geometry where the periodic poled domains, the superlattice, are aligned along $\hat{i}$, and the surface normal direction is along $\hat{j}$. The black and gray sections refer to the domains with inverted internal dipoles along the crystal optical axis. For TM-mode SPhPs, the electric field at the interface between the PSL crystal and the isotropic medium has to be polarized in i-j plane with components E_i and E_j, with the magnetic field pointing along $\hat{k}$.

the lithium niobate and lithium tantalate are taken into account in the calculations. For a $3m$ single crystal, the constant strain permittivity tensor, using the principal axes of the crystal as the basis, has the form

$$\boldsymbol{\epsilon}_S = \begin{bmatrix} \epsilon^S_{xx} & 0 & 0 \\ 0 & \epsilon^S_{xx} & 0 \\ 0 & 0 & \epsilon^S_{zz} \end{bmatrix}. \tag{1}$$

In our theoretical analysis we rely on the assumption that the superlattice-surface orientation axes (i,j,k) are aligned with the crystal principal axes (x,y,z). There are six possible superlattice-surface orientation combinations T_iN_j that can be formed by aligning different principal axes of the crystal to the superlattice orientation, $i,j \in \{x,y,z\}$ and $i \neq j$, as shown in Fig. 1.

II. DIELECTRIC RESPONSE OF PSL

To study the electromechanical coupling of a SPhP on a PSL, we start with the piezoelectric constitutive equations as proposed in previous theoretical analysis [38],

$$\begin{bmatrix} \boldsymbol{S} \\ \boldsymbol{D} \end{bmatrix} = \begin{bmatrix} \boldsymbol{s}_E & \boldsymbol{d}^t \\ \boldsymbol{d} & \boldsymbol{\epsilon}_T \end{bmatrix} \cdot \begin{bmatrix} \boldsymbol{\sigma} \\ \boldsymbol{E} \end{bmatrix}, \tag{2}$$

where $\boldsymbol{S}$ is the second-rank strain tensor which can be reduced and represented as a vector matrix,

$$\boldsymbol{S} = \begin{bmatrix} S_{xx} \\ S_{yy} \\ S_{zz} \\ S_{yz} \\ S_{zx} \\ S_{xy} \end{bmatrix}. \tag{3}$$

$\boldsymbol{\sigma}$ is the second-rank stress tensor which can also be reduced and represented as a vector matrix,

$$\boldsymbol{\sigma} = \begin{bmatrix} T_{xx} \\ T_{yy} \\ T_{zz} \\ T_{yz} \\ T_{zx} \\ T_{xy} \end{bmatrix}. \tag{4}$$

$\boldsymbol{D}$ is the electric displacement vector,

$$\boldsymbol{D} = \begin{bmatrix} D_x \\ D_y \\ D_z \end{bmatrix}. \tag{5}$$

$\boldsymbol{E}$ is the electric field vector,

$$\boldsymbol{E} = \begin{bmatrix} E_x \\ E_y \\ E_z \end{bmatrix}. \tag{6}$$

$\boldsymbol{s}_E$ is the fourth-rank elastic compliance tensor, which is the inverse of the fourth-rank elastic stiffness tensor $\boldsymbol{C}_E$, and can be reduced and represented as a 6×6 matrix. For a $3m$ point group crystal, the elastic stiffness tensor can be expressed as

$$\boldsymbol{s}_E^{-1} = \boldsymbol{C}_E = \begin{bmatrix} C_{11} & C_{12} & C_{13} & C_{14} & 0 & 0 \\ C_{12} & C_{11} & C_{13} & -C_{14} & 0 & 0 \\ C_{13} & C_{13} & C_{33} & 0 & 0 & 0 \\ C_{14} & -C_{14} & 0 & C_{44} & 0 & 0 \\ 0 & 0 & 0 & 0 & C_{44} & C_{14} \\ 0 & 0 & 0 & 0 & C_{14} & \frac{C_{11}-C_{12}}{2} \end{bmatrix}. \tag{7}$$

$\boldsymbol{d}$, as well as its transpose $\boldsymbol{d}^t$, are third-rank piezoelectric strain tensors which can be reduced and represented as

$$\boldsymbol{d} = \begin{bmatrix} 0 & 0 & 0 & 0 & d_{15} & -d_{22} \\ -d_{22} & d_{22} & 0 & d_{15} & 0 & 0 \\ d_{31} & d_{31} & d_{33} & 0 & 0 & 0 \end{bmatrix}. \tag{8}$$

$\boldsymbol{\epsilon}_T$ is the constant stress permittivity tensor,

$$\boldsymbol{\epsilon}_T = \begin{bmatrix} \epsilon^T_{11} & 0 & 0 \\ 0 & \epsilon^T_{11} & 0 \\ 0 & 0 & \epsilon^T_{33} \end{bmatrix}. \tag{9}$$

The piezoelectric constitutive equations, Eq. (2), can be rewritten in the stress form,

$$\boldsymbol{\sigma} = \boldsymbol{C}_E \cdot \boldsymbol{S} - \boldsymbol{e}^t \cdot \boldsymbol{E}, \tag{10a}$$

$$\boldsymbol{D} = \boldsymbol{e} \cdot \boldsymbol{S} + \boldsymbol{\epsilon}_S \cdot \boldsymbol{E}, \tag{10b}$$

where $\boldsymbol{e}$, and its corresponding transposed matrix $\boldsymbol{e}^t$, are the piezoelectric stress tensors,

$$\boldsymbol{e} = \boldsymbol{d} \cdot \boldsymbol{C}_E. \tag{11}$$

The periodically modulated piezoelectric coefficients along one of the crystal principal axes $x_i \in \{x,y,z\}$, for a single

period can be written as

$$\boldsymbol{e} \to \boldsymbol{e} f(x_i), \quad f(x_i) = \begin{cases} 1, & 0 \leqslant x_i < a, \\ -1, & a \leqslant x_i < l. \end{cases} \tag{12}$$

To analyze the piezoelectric equations, we consider the three-dimensional (3D) equation of motion with zero body force,

$$\nabla \cdot \boldsymbol{\sigma} = \rho \frac{\partial^2 \boldsymbol{u}}{\partial t^2}, \tag{13}$$

where ρ is the density and $\boldsymbol{u}$ is the displacement vector,

$$\boldsymbol{u} = \begin{bmatrix} u_x \\ u_y \\ u_z \end{bmatrix}, \tag{14}$$

which satisfies the strain-displacement relation,

$$\boldsymbol{S} = \nabla^t \cdot \boldsymbol{u}. \tag{15}$$

The divergence operator is defined as

$$\nabla \equiv \begin{bmatrix} \partial_x & 0 & 0 & 0 & \partial_z & \partial_y \\ 0 & \partial_y & 0 & \partial_z & 0 & \partial_x \\ 0 & 0 & \partial_z & \partial_y & \partial_x & 0 \end{bmatrix}, \tag{16}$$

where the spatial derivative components are $\partial_{x_i} \equiv \partial/\partial x_i$. ∇^t is the transpose matrix of the divergence. By substituting the equation of motion and the strain-displacement relation into Eq. (10) and taking the spatial derivative of Eq. (10a), we can obtain the piezoelectric equations in matrix representation [33],

$$\rho \frac{\partial^2}{\partial t^2} \boldsymbol{u} = -\hat{A}\boldsymbol{u} - i\hat{B}[f(x_i)\boldsymbol{E}], \tag{17a}$$

$$\boldsymbol{D} = f(x_i) i \hat{B}^t \boldsymbol{u} + \epsilon_0 \boldsymbol{\epsilon}_S \cdot \boldsymbol{E}, \tag{17b}$$

where the operators $\hat{A}$ and $\hat{B}$ are defined as

$$\hat{A}\boldsymbol{u} \equiv -\nabla \cdot \boldsymbol{C}_E \cdot \nabla^t \cdot \boldsymbol{u},$$
$$\hat{B}[f(x_i)\boldsymbol{E}] \equiv -i\nabla \cdot \boldsymbol{e}^t \cdot f(x_i)\boldsymbol{E}. \tag{18}$$

Equation (17a) describes the mechanical oscillation of the superlattice driven by an electric field. The oscillation, in turn, contributes to the electric displacement field within the superlattice, which is described by the first term on the right-hand side of Eq. (17b). The overall dielectric response to the electric field including the contribution from the mechanical oscillation can be solved with these coupled equations. To obtain an expression for the dielectric response near each lattice wave resonance, we transform the displacement and the electric field to momentum space, and take the Fourier series expansion of the piezoelectric modulation,

$$\boldsymbol{u} = \int \boldsymbol{u}_q e^{i(\boldsymbol{q}\cdot\boldsymbol{r}-\omega t)} d^3\boldsymbol{q}, \tag{19a}$$

$$\boldsymbol{E} = \int \boldsymbol{E}(\boldsymbol{k}) e^{i(\boldsymbol{k}\cdot\boldsymbol{r}-\omega t)} d^3\boldsymbol{k}, \tag{19b}$$

$$f(x_i) = \sum_{m\neq 0} F_m e^{iG_m x_i}, \tag{19c}$$

where

$$G_m \equiv \frac{2\pi m}{l},$$
$$F_m \equiv \frac{2\sin\frac{m\pi a}{l}}{m\pi} e^{-i\frac{m\pi a}{l}}. \tag{20}$$

We substitute the solution of $\boldsymbol{u}$ in terms of $\boldsymbol{E}$ near the mth resonant frequency ω_m, obtained from Eq. (17a), into Eq. (17b). It is important that the piezoelectric modulated phase of the electromagnetic field matches the mechanical wave to support a SPhP that can propagate over many wavelengths. The modulated piezoelectric effect and quasiphase matching have been extensively studied for the frequency conversion of light. The condition of perfect phase matching is difficult to achieve but propagating excitations can exist if the phase matching condition is approximately satisfied, i.e., quasiphase matching,

$$\boldsymbol{q} \simeq \boldsymbol{k} + \boldsymbol{G}_m, \tag{21}$$

where $\boldsymbol{G}_m = G_m \hat{x}_i$. For a wavelength of the electromagnetic wave much larger than the poling period of the PSL, an explicit expression of the electric displacement in terms of the electric field can be written out. This "so-called" long-wavelength approximation is well satisfied for our system since the SPhP wavelength is on the order of a centimeter and the poling period is on the order of a micrometer. In the long-wavelength approximation,

$$k \ll G_m \quad \text{and} \quad f(x_i)e^{iG_m x_i} \approx \langle f(x_i)e^{iG_m x_i}\rangle. \tag{22}$$

By applying the quasiphase matching condition and the long-wavelength approximation [26], the final result for the electric displacement is

$$\boldsymbol{D} = [-2|F_m|^2 \hat{B}_m^t(\omega^2\rho\hat{I} - \hat{A}_m)^{-1}\hat{B}_m + \epsilon_0\boldsymbol{\epsilon}^S]\boldsymbol{E}. \tag{23}$$

Equation (23) contains the resulting dielectric response tensor $\boldsymbol{\epsilon}$, where $\boldsymbol{D} = \epsilon_0\boldsymbol{\epsilon}\boldsymbol{E}$,

$$\boldsymbol{\epsilon} = \boldsymbol{\epsilon}^S - 2\frac{|F_m|^2}{\epsilon_0}\hat{B}_m^t(\omega^2\rho\hat{I} - \hat{A}_m)^{-1}\hat{B}_m. \tag{24}$$

The dielectric response of the PSL, $\boldsymbol{\epsilon}$, is the essential quantity needed to calculate the dispersion relation of the supported SPhPs. $\boldsymbol{\epsilon}$ determines the coupling between the dipole excitations and the electromagnetic waves within the crystal. The second term on the right side of Eq. (24) includes the frequency dependence of the dielectric response of the PSL. The mechanical properties are described by $\hat{A}_m$. The modulated piezoelectric effect enters the equation in the coefficient F_m. $\hat{B}_m$ gives the coupling between the electric field and mechanical vibration. For an isotropic crystal surface in vacuum, a negative dielectric response of the crystal results in an evanescent electromagnetic field along the surface normal direction, and the corresponding SPhP dispersion relation is straightforward to calculate analytically. However, our SPhP analysis has to adapt the complex dielectric response given by Eq. (24), due to the more complicated crystal structure of the anisotropic PSL, to calculate the SPhP dispersion relations.

III. SMALL ROTATION APPROXIMATION

The dielectric response $\boldsymbol{\epsilon}$, obtained from Eq. (24), is not in general a diagonal matrix in the basis along the crystal principal axes. The off-diagonal parts of the dielectric response are introduced by the second term in Eq. (24) due to the piezoelectrically induced superlattice vibrations. The surface polariton dispersion relation on a general anisotropic surface can be calculated as shown in Ref. [34]. However, a simple analytic solution of the dispersion relation only exists for TM-mode SPhPs [27]. Therefore, it is convenient to approximate the general SPhPs as TM-mode SPhPs on PSL surfaces. A diagonalized dielectric response is required for a TM-mode SPhP dispersion relation calculation. For periodically poled $3m$ crystals, the dielectric response along the crystal principal axes,

$$\boldsymbol{\epsilon} = \begin{bmatrix} \epsilon_{xx} & 0 & 0 \\ 0 & \epsilon_{yy} & \epsilon_{yz} \\ 0 & \epsilon_{yz} & \epsilon_{zz} \end{bmatrix}, \tag{25}$$

can be diagonalized by a rotation operator,

$$\hat{R} = \begin{bmatrix} 1 & 0 & 0 \\ 0 & \cos\theta & -\sin\theta \\ 0 & \sin\theta & \cos\theta \end{bmatrix}. \tag{26}$$

The diagonalized dielectric response matrix has the form

$$\boldsymbol{\epsilon}' = \hat{R}^{-1}\boldsymbol{\epsilon}\hat{R} = \begin{bmatrix} \epsilon_x & 0 & 0 \\ 0 & \epsilon_y & 0 \\ 0 & 0 & \epsilon_z \end{bmatrix}. \tag{27}$$

The angle θ shown in Fig. 2, between the dielectric response principal axes (x',y',z') of a PSL and the crystal principal axes (x,y,z) of the corresponding single crystal, can be derived from the rotation operator,

$$\tan(2\theta) = \frac{2\epsilon_{yz}}{\epsilon_{yy}-\epsilon_{zz}} \Rightarrow \theta = \frac{1}{2}\arctan\frac{2\epsilon_{yz}}{\epsilon_{yy}-\epsilon_{zz}}. \tag{28}$$

In a typical PPLN or PPLT crystal, the superlattice-surface orientation axes are aligned with the crystal principal axes $(i,j,k) \in (x,y,z)$. For a small rotation angle $|\theta| \ll 1$, the rotated dielectric principal axes (x',y',z') are almost aligned with the crystal principal axes (x,y,z). We refer to the condition $(x',y',z') \sim (x,y,z)$ as the small rotation approximation (SRA). It leads to a simplification of the calculations of the SPhP dispersion relations. We validate this approximation later in this work by comparing its result with an exact numerical calculation for PPLN and PPLT.

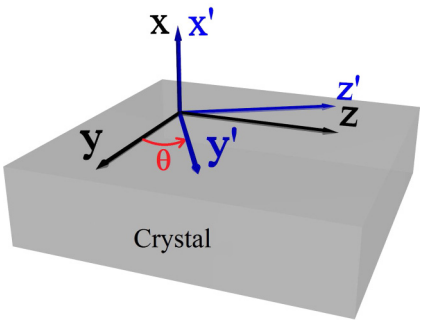

FIG. 2. Rotation of a $3m$ single crystal in y-z plane around the crystal principal axis x with an angle θ required to diagonalize the dielectric response matrix of a PSL.

IV. TM-MODE SPhP DISPERSION RELATION

The calculated dielectric response of PSL crystals for different T_iN_j orientations includes the electromechanical couplings between the phonon vibrations and the TM-mode photons. The dispersion relation describes the coupled photon-phonon mixture (polariton) traveling within the material. On the surface of the material, the TM waves due to the boundary discontinuity can be confined to the surface with an exponentially decaying electromagnetic field normal to the surface. Therefore, it is useful to analyze the dispersion relation of the SPhPs to study the properties of the confined polaritons traveling along a surface.

The dielectric response along the different axes are generally not the same. To include the anisotropy in the SPhP dispersion relation calculation, we take advantage of previous work on semi-infinite anisotropic crystals. The TM-mode SPhPs only exist on the T_iN_j surfaces where one of the principal axes of the diagonalized dielectric response is aligned with the magnetic field direction $\hat{k}$, and the plane defined by the other two principal axes is obtained by a rotation of the i-j plane around the k axis. The corresponding TM-mode real SPhP dispersion relation is given by [27]

$$k_i^2 = \frac{\omega^2}{c^2}\epsilon_M\frac{\epsilon_i\epsilon_j - \epsilon_M\epsilon_{jj}}{\epsilon_i\epsilon_j - \epsilon_M^2}, \tag{29}$$

where ϵ_i, $\epsilon_j \in \{\epsilon_x,\epsilon_y,\epsilon_z\}$, as defined in Eq. (27), are the two principal dielectric response along the directions near the superlattice direction $\hat{i}$ and the surface normal direction $\hat{j}$, respectively. $\epsilon_{jj} \in \{\epsilon_{11},\epsilon_{22},\epsilon_{33}\}$ is the dielectric response on the diagonal of the dielectric response matrix, which describes the response to the electric field along the surface normal direction $\hat{j}$, and ϵ_M is the dielectric permittivity of the isotropic medium. There are two different types of SPhPs described by this dispersion relation. A real SPhP has a resonance at ω_R where the group velocity of the surface wave is zero,

$$\epsilon_i(\omega_R)\epsilon_j(\omega_R) - \epsilon_M^2 = 0. \tag{30}$$

For a confined, nonradiative SPhP, the wave number along the propagation direction is real while the wave numbers along the surface normal direction are required to be imaginary. With these frequency requirements on the wave numbers, the condition for a TM-mode, real SPhP can be obtained by examining the existence of a SPhP resonance $\omega = \omega_R$, which satisfies Eq. (30) [27,39],

$$\epsilon_i(\omega) < 0 \quad \text{and} \quad \epsilon_j(\omega) < \frac{\epsilon_M^2}{\epsilon_i(\omega)}. \tag{31}$$

Outside the real SPhP regime, there is another set of frequency ranges that fulfills the wave number requirements without any SPhP resonance [40],

$$\epsilon_i(\omega) < 0 \quad \text{and} \quad \epsilon_j(\omega) > 0. \tag{32}$$

The corresponding dispersion is given by the same equation, Eq. (29), as the real SPhP, but a different constraint. For the frequencies that satisfy Eq. (32), the dispersion curves represent virtual SPhPs. Unlike real SPhPs, the group velocity of a virtual SPhP can be very small but not zero. This implies that virtual SPhPs have no resonant surface polariton excitation. They only exist for finite wave numbers and in the presence of an associated driving field [41–43]. The dispersion relations of virtual TM-mode SPhPs are bounded between the light line in the isotropic medium and the dispersion curve of the bulk polariton polarized along the surface normal direction in the crystal [44]. All TM-mode, virtual SPhPs terminate at the natural frequency of the corresponding longitudinal optical phonons ω_{LO}, where the polariton inside the crystal behaves like a bulk mode polariton, no longer confined to the surface.

For our analytic calculation on the T_iN_j surfaces, since Eq. (29) requires that the magnetic field direction $\hat{k}$ lies parallel to one of the dielectric principal axis $\{\hat{x},\hat{y},\hat{z}\}$, the allowed rotation required to diagonalize the dielectric response matrix is in the i-j plane. Therefore, Eq. (29) is valid only for T_yN_z and T_zN_y orientations with a dielectric response shown in Eq. (25). For the other four orientations we have to make the assumption that the rotation is negligible, the SRA, in order to get an analytic SPhP dispersion relation if rotation is required to diagonalize the corresponding dielectric response matrix. In these cases, the magnetic field is almost aligned with one of the dielectric principal axes. To apply the analytic calculation to different superlattice-surface orientations, we use Eq. (29) to calculate the SPhP dispersion relations for the cases where one of the principal axes of the dielectric response is perfectly aligned with the magnetic field and apply the SRA to derive a simple analytic dispersion relation for other cases. Under the SRA, $\epsilon_{jj} \simeq \epsilon_j$, the dispersion relation becomes

$$k_i^2 \simeq \frac{\omega^2}{c^2}\epsilon_j\epsilon_M\frac{\epsilon_i-\epsilon_M}{\epsilon_i\epsilon_j-\epsilon_M^2}. \tag{33}$$

The wave vector along the surface normal direction in the isotropic medium and in the crystal under the SRA can be simplified to

$$k_{Mj}^2 = \frac{\omega^2}{c^2}\epsilon_M - k_i^2, \tag{34a}$$

$$k_j^2 \simeq \frac{\epsilon_i}{\epsilon_j}\left(\frac{\omega^2}{c^2}\epsilon_j - k_i^2\right). \tag{34b}$$

Within the SRA, the Maxwell wave equation for a TM-mode electromagnetic wave leads to a simple relation between the electric field components along the propagation direction and the surface normal direction in the two dielectric materials at the interface [39],

$$k_iE_i + k_{Mj}E_{Mj} = 0, \tag{35a}$$

$$k_i\epsilon_iE_i + k_j\epsilon_jE_j = 0. \tag{35b}$$

With the wave vectors given by Eqs. (33) and (34), the relative electric field components near the interface can be obtained from Eq. (35). The plane wave solution of the electric field has to be an evanescent wave along the surface normal direction $k_{Mj}^2 < 0$ and $k_j^2 < 0$, for the existence of surface polaritons. This restriction further narrows the valid virtual SPhP frequency ranges defined in Eq. (32). For an isotropic media with a positive dielectric permittivity $\epsilon_M > 0$, the overall constraint for TM-mode virtual SPhPs is [41]

$$\epsilon_i(\omega) < 0 \quad \text{and} \quad \epsilon_j(\omega) > \epsilon_M. \tag{36}$$

According to Eq. (35b), two types of TM-mode SPhP, real and virtual, with different range of dielectric response, Eqs. (31) and (36), respectively, have distinct electric field distributions near the interface.

The exact dispersion relation for SPhPs on T_xN_y, T_xN_z, and T_yN_x surfaces of PPLN and PPLT can also be calculated numerically without the SRA. For estimating the validity of the SRA, we calculate and analyze the exact dispersion relation at sample frequencies within the valid SPhP domain using Eqs. (6) and (17) in [34]. As the dielectric principal axis rotates away from $\hat{k}$, the electric field will have a nonzero electric field component along $\hat{k}$ to satisfy the electromagnetic wave equation. The electric field rotates out of the i-j plane. A TE polarized component is generated and the excitation becomes a hybrid TM-TE mode. However, in the cases described here, the TE component is small as can be seen through the agreement between the analytic and exact numerical calculations of the dispersion relations for the excitations. The analytic calculation assumes the SPhP is pure TM polarized. Therefore, without the SRA, we would not be able to compute the dispersion relations analytically as TM-mode SPhPs anymore. This leads to an electromagnetic wave with two superposed modes (k_{j1} and k_{j2}) in the crystal along the surface normal direction. If both modes of the electromagnetic wave have evanescent surface normal components (both k_{j1} and k_{j2} have positive imaginary parts), the SPhP is confined at the PSL surface and propagates along the superlattice direction. If one of the two surface normal electromagnetic wave modes describes a propagating field (either k_{j1} or k_{j2} is real or has a negative imaginary part), the polariton will radiate along the surface normal direction into the crystal. The energy radiated by the SPhP causes the excitation to decay as it propagates along the surface of the PSL. The radiative decay introduces an intrinsic damping for these SPhPs. This type of SPhP has been termed as pseudo-SPhP [27]. A pseudo-SPhP will lose energy and attenuate as it propagates along a crystal surface.

V. NUMERICAL ANALYSIS

We calculate the dielectric response matrices using Eq. (24) with the parameters listed in Table I [36,45,46] at room temperature, 25 ° C, assuming the artificial superlattice constant, or domain period, to be $l = 7.2\,\mu$m. For simplicity we consider homogeneous inverted domains with constant domain width equal to half of the superlattice constant, $a = l/2 = 3.6\,\mu$m. The nonzero contributions of the electromechanical coupling to the dielectric response are near the odd order resonances which correspond to the odd order terms of the Fourier expansion shown in Eq. (19c). Only the dielectric response near the first order resonances is presented in our report, which corresponds to $m = 1$ in Eq. (24). The dielectric response near the higher order resonances at higher frequencies can be computed in the same manner with different m values. For semi-infinite PSLs in vacuum, where $\epsilon_M = 1$, the supported

TABLE I. A list of numerical values of the parameters used for the calculations. The absolute quantities are measured at room temperature, 25 °C. The temperature coefficients α and β are the coefficients of the polynomial expansion of the ratio of the corresponding absolute quantities Q measured at temperature T to the quantities measured at 25 °C: $\frac{Q(T)}{Q(25)} = 1 + \alpha(T-25) + \beta(T-25)^2$. For lithium niobate, the small second order temperature dependence β can be neglected except for the thermal expansion coefficients. The temperature coefficients of the elastic stiffness, the piezoelectric constant, and the dielectric permittivity are found in [45], valid within the range 0–110 °C. The thermal expansion coefficients are found in [46], valid within the range 25–500 °C.

	$LiNbO_3$		$LiTaO_3$		
	Absolute quantities	Normalized temperature coeff.	Absolute quantities	Normalized temperature coeff.	
Constant electric field elastic stiffness	($\times 10^{11}$ N/m^2)	α ($\times 10^{-4}$/°C)	($\times 10^{11}$ N/m^2)	α ($\times 10^{-4}$/°C)	β ($\times 10^{-7}$/°C^2)
c_{11}^E	2.030	− 1.74	2.298	− 1.03	0.77
c_{12}^E	0.573	− 2.52	0.440	− 3.41	− 1.18
c_{13}^E	0.752	− 1.59	0.812	− 0.50	6.00
c_{14}^E	0.085	− 2.14	− 0.104	6.67	16.7
c_{33}^E	2.424	− 1.53	2.798	− 0.96	− 3.21
c_{44}^E	0.595	− 2.04	0.968	− 0.43	1.67
c_{66}^E	0.728	− 1.43	0.929	− 0.47	1.24
Piezoelectric strain constants	($\times 10^{11}$ C/N)	($\times 10^{-4}$/°C)	($\times 10^{11}$ C/N)	($\times 10^{-4}$/°C)	($\times 10^{-7}$/°C^2)
d_{15}	6.92	3.45	2.64	− 1.31	− 9.64
d_{22}	2.08	2.34	0.75	− 1.32	− 9.79
d_{31}	− 0.085	19.1	− 0.30	3.27	43.1
d_{33}	0.60	11.3	0.57	2.74	118
Constant strain dielectric permittivity		($\times 10^{-4}$/°C)		($\times 10^{-4}$/°C)	($\times 10^{-7}$/°C^2)
$\epsilon_{11}^S/\epsilon_0$	44.3	3.23	42.6	3.29	4.28
$\epsilon_{33}^S/\epsilon_0$	27.9	6.27	42.8	11.6	78
Thermal expansion for different crystal orientation	Expansion coefficients			Expansion coefficients	
	α ($\times 10^{-5}$/°C)	β ($\times 10^{-9}$/°C^2)		α ($\times 10^{-5}$/°C)	β ($\times 10^{-9}$/°C^2)
X cut	1.44	7.1		1.61	7.5
Y cut	1.59	4.9		1.54	7.0
Z cut	0.75	− 7.7		0.22	− 5.9

SPhP dispersion relations are calculated using Eq. (33) for different superlattice-surface orientations in the regimes where the SRA is valid.

A. Dielectric response matrix

The calculated dielectric response matrix elements (ϵ_{xx}, ϵ_{yy}, ϵ_{zz}, and $\epsilon_{yz} = \epsilon_{zy}$) are plotted in Fig. 3 for PPLN surfaces and in Fig. 4 for PPLT surfaces. For each superlattice-surface orientation, the three solid lines in the figure represent the diagonal elements of the dielectric response matrices. The off-diagonal elements are plotted using dashed lines. The basis used to calculate the matrices are along the crystal principal axes which are assumed to be aligned with the superlattice-surface axes for our theoretical setup shown in Fig. 1. For further analytic SPhP dispersion calculations under the SRA, the small off-diagonal elements in the dielectric response matrix are neglected.

We obtain the diagonalized dielectric response matrices and the corresponding rotation angles by Eqs. (27) and (28). The matrix elements of the diagonalized dielectric response are shown in Fig. 5 for PPLN surfaces and in Fig. 6 for PPLT surfaces. This diagonalization process mixes the dielectric response along the crystal principal y axis (the red curves) with the dielectric response along the crystal optical z axis (the black curves) when a rotation is required to diagonalize the matrix. The valid frequency ranges for SPhPs are calculated from the dielectric response constraints for both real, Eq. (31), and virtual, Eq. (36), SPhPs. We record the angle of rotation for diagonalization to check the validity of the SRA for each valid SPhP frequency domain.

B. SPhP dispersion relation curves

Due to the constraints for a real SPhP, requiring both the dielectric response along the propagation and the surface normal directions to be negative at the same frequency, real SPhPs exist on both PPLN and PPLT surfaces only with $T_y N_x$ superlattice-surface orientation. The solid curve in Fig. 7 shows the calculated dispersion relation of the real SPhP on the PPLN surface under the SRA. The valid frequency range for the real SPhP is from 549.74 to 594.25 MHz. The

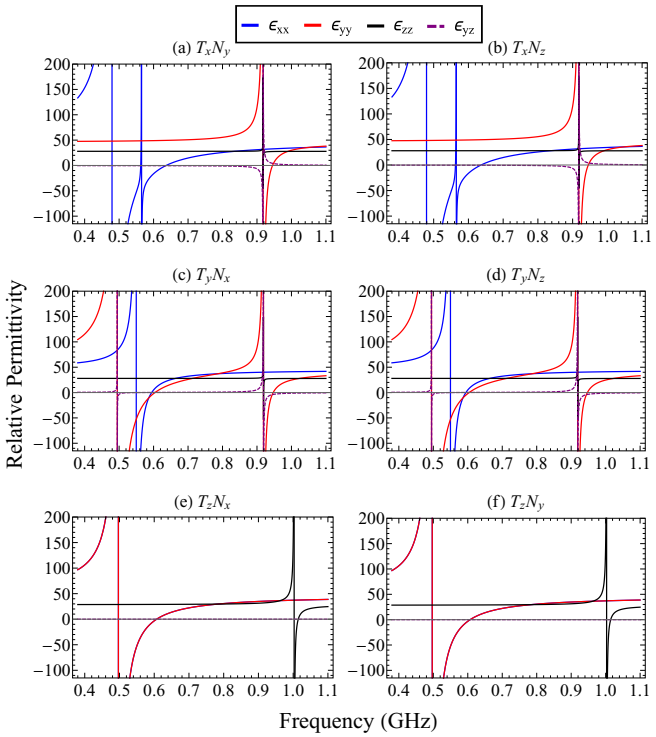

FIG. 3. Calculated dielectric response matrix elements *before diagonalization* with respect to different frequencies for the six different superlattice-surface orientations. Matrix element ϵ_{ij} describes the dielectric response along the crystal principal axis $i \in \{x,y,z\}$ to the electric field polarized along the principal axis $j \in \{x,y,z\}$. $\epsilon_{xy} = \epsilon_{yx} = \epsilon_{xz} = \epsilon_{zx} = 0$ and $\epsilon_{yz} = \epsilon_{zy}$ as shown in Eq. (25). For the two equivalent orientations shown in (e) and (f), ϵ_{xx} and ϵ_{yy} are the same, due to the uniaxial behavior of the $3m$ crystals.

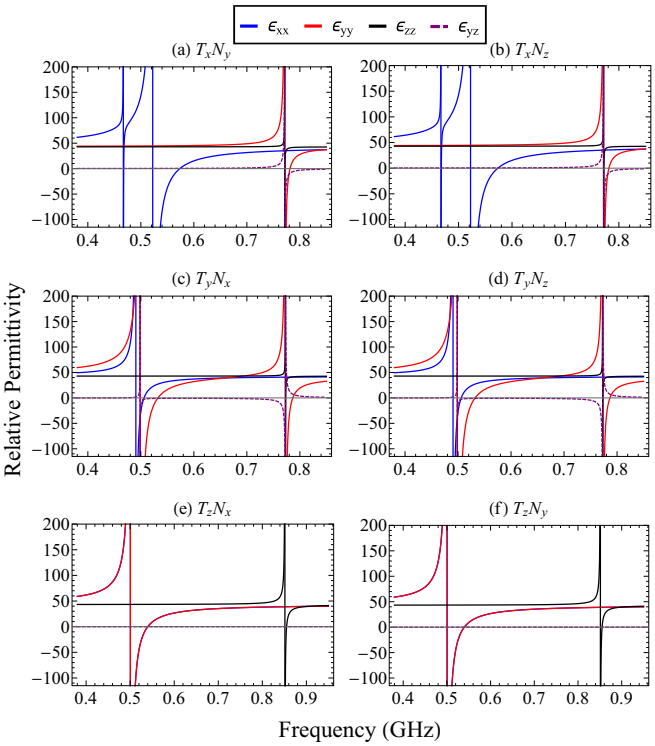

FIG. 4. Calculated matrix elements of 3-by-3 PPLT dielectric response matrices *before diagonalization* are shown in the same layout as Fig. 3 for PPLN. As a $3m$ class crystal, lithium tantalate has the same uniaxial behavior as lithium niobate. Hence, PPLT also has dielectric response matrices in the form shown in Eq. (25).

rotation angles required to diagonalize the dielectric response matrix are negligible within this range, $|\theta| < \pi/400 \ll 1$. The group velocity of the SPhP goes to zero as the frequency approaches the real SPhP resonance at 594.25 MHz. Figure 8 shows the calculated dispersion relation of the real SPhP on the PPLT surface. The real SPhP exists in the frequency range from 498.55 MHz to its resonance at 505.99 MHz. The corresponding rotation angles needed to diagonalize the dielectric response matrix are also negligible within the valid real SPhP domain, $|\theta| < \pi/200 \ll 1$. The exact numerical calculations at sample frequencies within the valid domain, shown with red crosses, confirm the SRA on both the PPLN and PPLT surfaces.

The exact numerical analysis shows that a small rotation of the dielectric response principal axes around the surface normal direction adds a tiny positive imaginary part to the approximated wave vector along the superlattice direction. This intrinsic damping along the SPhP propagation direction suggests that the SPhPs we analytically approximated under the SRA are indeed pseudo-SPhPs. A small propagating mode in the crystal is discovered along the surface normal direction. We compute the energy loss of the surface polariton and the radiation energy carried by the propagating electromagnetic field component along the surface normal direction by integrating the time averaged Poynting vector over the planes perpendicular to the superlattice direction and the planes parallel to the crystal surface at the sample frequencies. It is confirmed that the damped SPhPs radiate their energy into the PSL. For a small rotation angle, the imaginary part of the wave vector along the superlattice direction is orders of magnitude smaller than the real part. For the real SPhP in our analysis on PPLN surface $|\frac{\mathrm{Im}[k_i]}{\mathrm{Re}[k_i]}| < 10^{-3}$, and on the PPLLT surface $|\frac{\mathrm{Im}[k_i]}{\mathrm{Re}[k_i]}| < 10^{-4}$. The SPhPs can propagate along the surface for many wavelength before they lose substantial energy.

In addition to the real SPhPs, Figs. 9 and 10 show that virtual SPhPs exist on the PPLN and PPLT surfaces. For a virtual SPhP, the diagonalized dielectric response near the propagation direction is negative, $\epsilon_x < 0$, but is required to be positive near the surface normal direction, $\epsilon_z > 0$. The finite wave numbers of the corresponding virtual SPhPs are listed above each dispersion relation curve in Figs. 9 and 10. The SRA is applied for approximating the dispersion relations using Eq. (33) on the T_xN_y, T_xN_z, and T_yN_x surfaces. The rotation angles $|\theta| < \pi/20$ on the PPLN surfaces and $|\theta| < \pi/12$ on the PPLT surfaces are also small. Since there is no rotation required to diagonalize the dielectric response matrix on the T_zN_x surface, TM-mode SPhPs are supported. Therefore, the analytic calculation using Eq. (29) is performed to obtain the dispersion curves on the T_yN_z, T_zN_x, and T_zN_y surfaces. It is interesting to note that there are two "almost photonlike" virtual SPhPs on the PPLN surfaces shown in Figs. 9(c) and 9(g). The absolute value of the

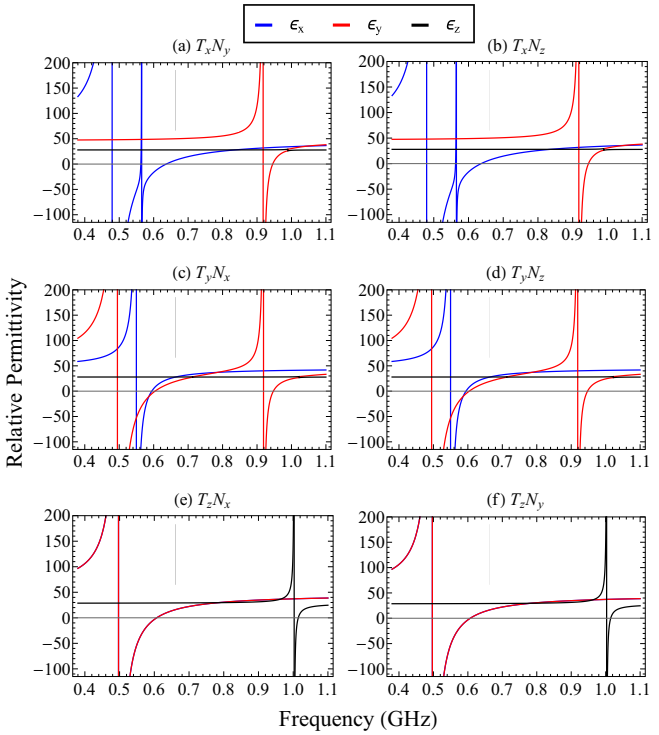

FIG. 5. The *diagonalized* dielectric response matrix elements with respect to different frequencies of PPLN crystals are shown in the same layout as Fig. 3. Matrix element ϵ_α is the dielectric response along the new rotated axis $\alpha \in \{x', y', z'\}$ to the electric field polarized along the same direction $\hat{\alpha}$. Unlike Fig. 3, only the three matrix elements along the diagonal are nonzero.

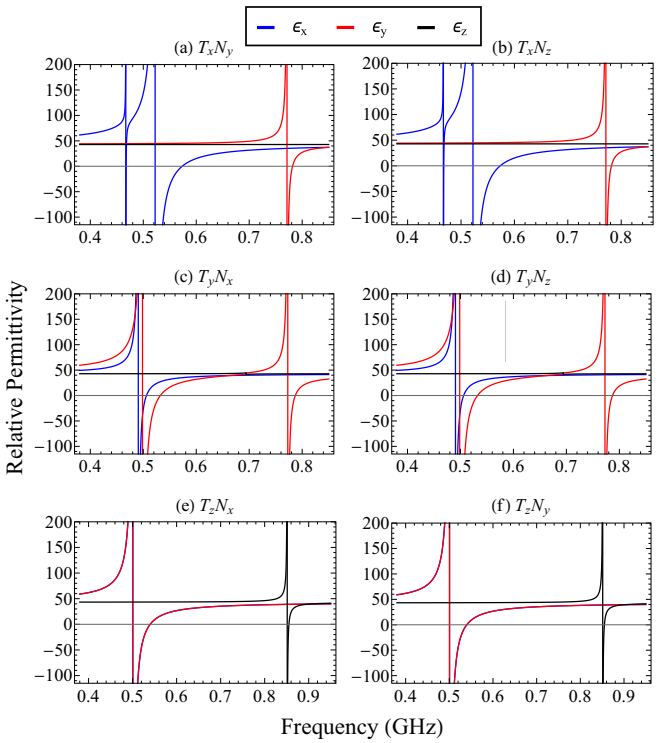

FIG. 6. The *diagonalized* dielectric response along the new rotated axes of PPLT crystals is shown in the same layout as Fig. 5 for PPLN.

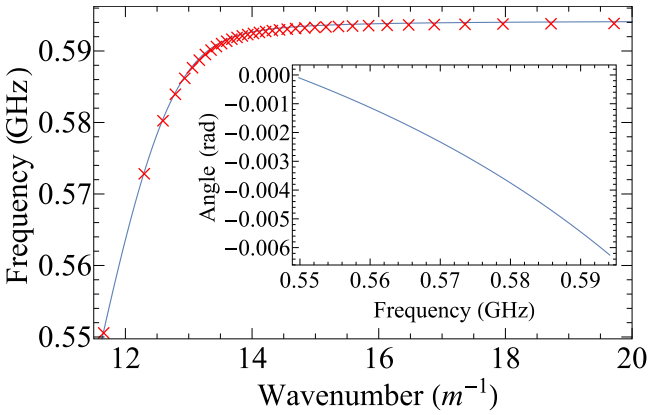

FIG. 7. The dispersion relation of the real SPhP calculated under the SRA on the T_yN_x surface of PPLN. The corresponding rotation angle required to diagonalize the dielectric response matrix is shown. The numerical analysis of the dispersion relation without the SRA is plotted in red crosses for comparison.

dielectric response is much greater than the vacuum dielectric permittivity in the frequency ranges where these two virtual SPhPs exist. These SPhPs are primarily photon excitations. They behave like surface guided light waves.

Similar to real SPhPs, the virtual SPhPs on the T_xN_y, T_xN_z, and T_yN_x surfaces are also pseudosurface polaritons with small intrinsic damping along the propagation direction. Comparing the dispersion relations computed by the exact numerical calculation (red crosses) to the dispersion curves obtained by the analytic calculation with the SRA (solid curves), the calculations agree well for most of the virtual SPhPs. The maximum rotation angle occurs for the T_yN_x surface of PPLN [Fig. 9(i)] and on the T_xN_y or the T_xN_z surfaces of PPLT [Fig. 10(a) or 10(d)]. The maximum errors for the virtual SPhP propagation wave number of the SRA in the cases with relatively large rotations are less than 10% .

The electric field distribution of a real SPhP and a virtual SPhP near the interface between vacuum and the PPLN crystal is shown in Figs. 11 and 12, respectively. The SPhPs on the PPLT surfaces have the similar electric field distribution. The relative vector field is calculated using Eq. (35) with

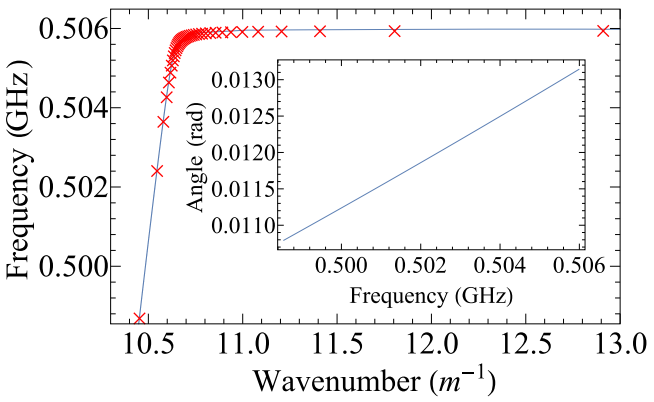

FIG. 8. The dispersion relation obtained with the SRA on the T_yN_x surface of PPLT. Similar to Fig. 7, the corresponding rotation angles are shown, and the results of the numerical analysis are plotted in red crosses for PPLT.

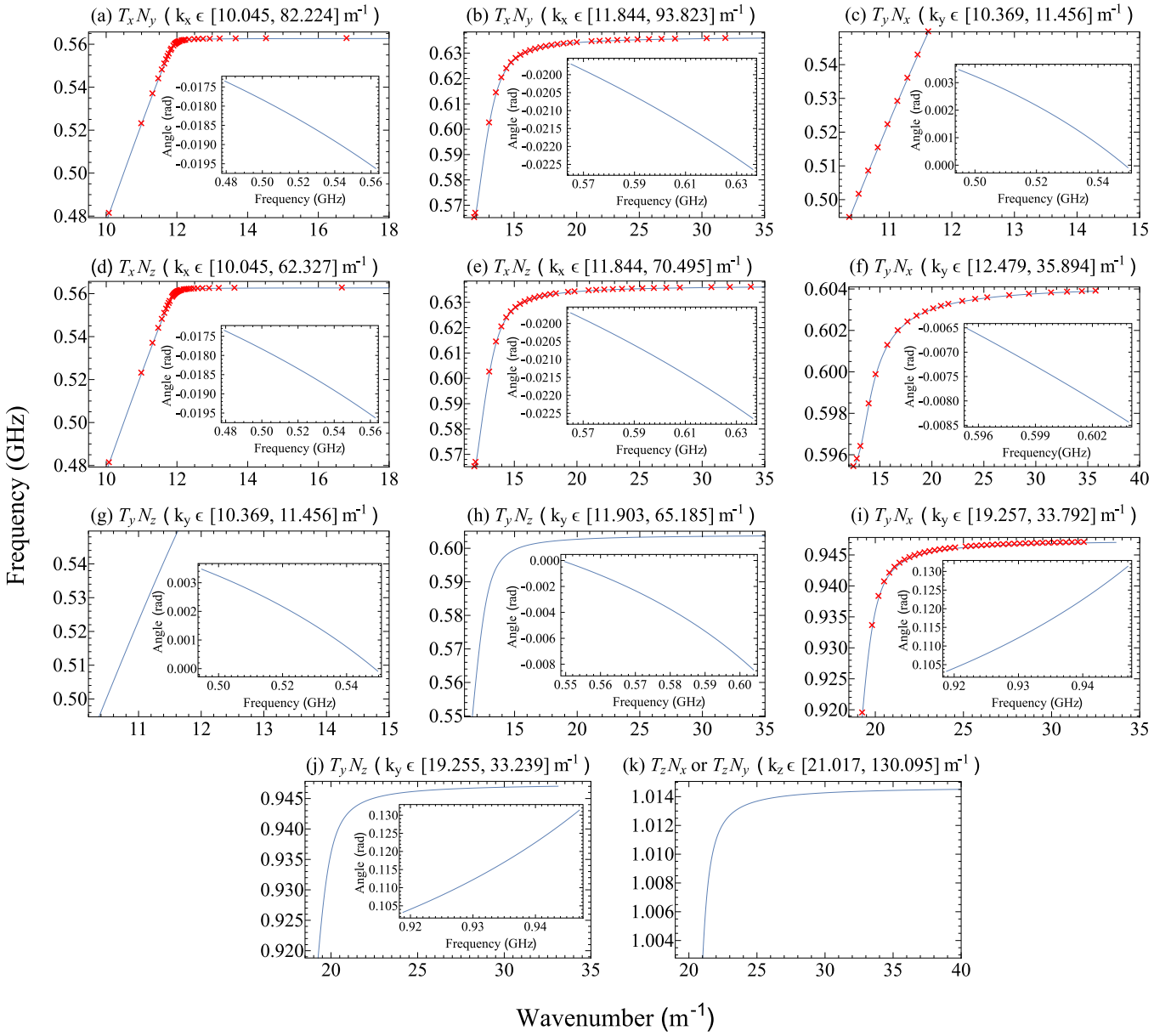

FIG. 9. The dispersion relations of 12 possible virtual SPhPs on T_iN_j surfaces of PPLN. The SRA is applied to obtain the dispersion curves (solid lines) on the T_xN_y, T_xN_z, and T_yN_x surfaces. Similar to Figs. 7 and 8, the results of the corresponding numerical calculation without the SRA in red crosses and the rotation angle required to diagonalize the dielectric response matrix are also shown. The dispersion relations on the T_yN_z, T_zN_x, and T_zN_y surfaces are obtained by the analytic calculation for TM-mode SPhPs. Since the T_zN_x and the T_zN_y orientations are equivalent, only one of the two identical dispersion curves is displayed, and the corresponding rotation angles are zero (the dielectric response matrices are naturally diagonalized along the superlattice-surface orientation). The corresponding allowed range of the virtual SPhP propagation wave number calculated under the SRA is listed above each dispersion curve.

the wave vector components given by Eqs. (33) and (34) under the SRA. The field amplitude is normalized to unity at the interface. There is a $\pi/2$ phase difference between the electric field components along the propagation and the surface normal directions. This phase difference causes the rotation of the electric field vector along the propagation direction and can be understood by imposing pure imaginary wave vector components along the surface normal direction in Eq. (35). The electromagnetic wave associated with the real SPhP propagates along the interface and exponentially decays away from it. The confined polariton along the surface is illustrated as the electric field amplitude distribution concentrates at the interface, the bright red area near the zero-distance line, shown in Fig. 11 for a real SPhP. Closer to its resonance at ω_R, the real SPhP is more confined to the surface of the PSL. On the other hand, as shown in Fig. 12, the strength of the electromagnetic field close to the interface in the vacuum is always stronger than or equal to the field in the PSL for a virtual SPhP. Closer to its stop point, where the virtual SPhP terminates at ω_{LO}, the polariton is less confined to the surface of the PSL and behaves like a bulk polariton inside the PSL at the stop point. The calculated electric field vectors are slightly off the plane

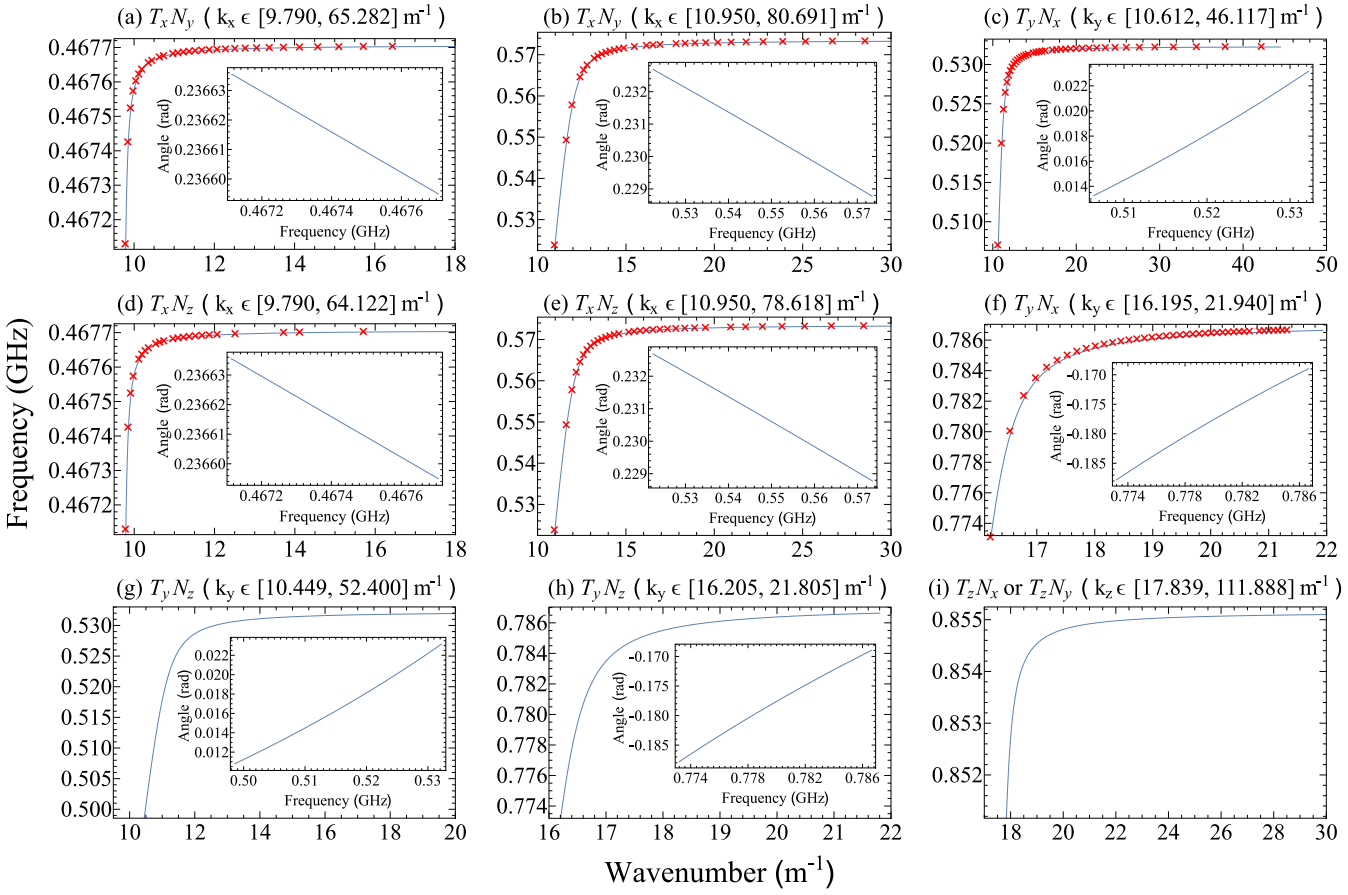

FIG. 10. The dispersion relations of nine possible virtual SPhPs on T_iN_j surfaces of PPLT and the corresponding rotation angles are shown in the same layout as Fig. 9. The results of the numerical analysis in red crosses are displayed on top of some of the dispersion curves which are obtained under the SRA.

defined by the propagation and the surface normal directions, shown in Figs. 11 and 12, and the field amplitude is slowly damped along the propagation direction, in the full calculation without the SRA.

C. SPhP resonance frequency tunability

All the parameters used in our calculations are measured at room temperature, 25 ° C, and on the surface of PSLs with a fixed poling period of 7.2 μm. In order to tune the SPhP resonance frequencies, we examined the effect of

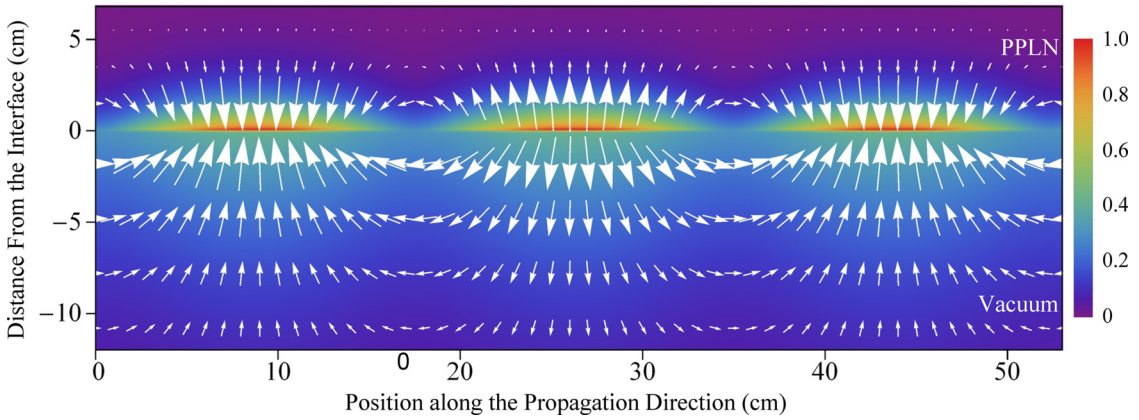

FIG. 11. The electric field pattern calculated under the SRA for the *real* SPhP near the T_yN_x surface of PPLN at 594.02 MHz. The horizontal axis, at distance $d = 0$, indicates the interface. The electric field pattern inside the PPLN (vacuum) is shown above (below) the interface, in the positive (negative) distance region as labeled in the figure. The length of the vectors, shown by white arrows, indicates the field strength at the center of each arrow. The density distribution of the relative vector field amplitude is shown in the colored background. The electric field exponentially decays away from the interface.

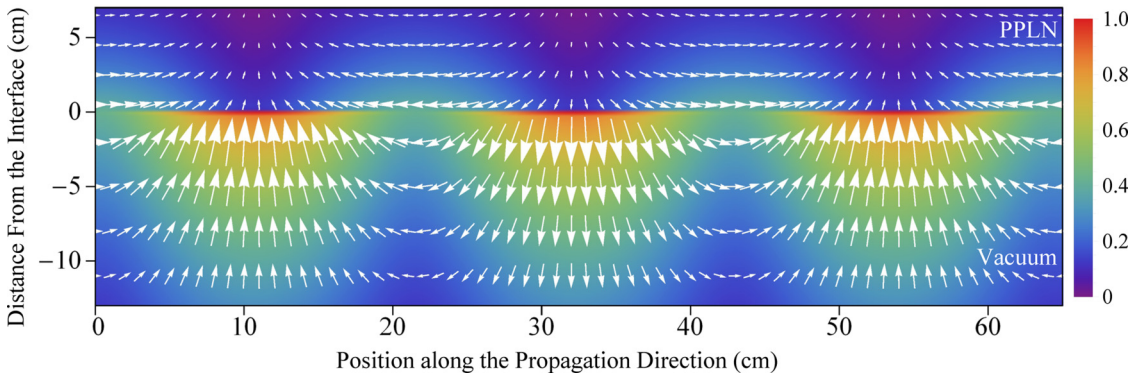

FIG. 12. The *virtual* SPhP electric field pattern near the T_yN_x surface of PPLN at 599.87 MHz under the SRA. Unlike the real SPhP, the electromagnetic field strength in the vacuum close to the interface is always stronger than or equal to the field strength in the PSL for the virtual SPhPs.

different temperatures and superlattice constants on our SPhP calculations. Due to the small temperature dependence of all the parameters shown in Table I, the overall modification of the SPhPs due to temperature variation is small but not insignificant for atom-surface interaction. The resonant frequency of the real SPhP on the T_yN_x surface of PPLN varies from 594.25 MHz at 25 ° C to 589.75 MHz at 110 ° C. The resonant frequency of the real SPhP dispersion relation on the PPLT surface varies from 505.99 MHz at 25 ° C to 503.82 MHz at 110 ° C. For such small temperature dependencies, it is difficult to tune the resonant frequencies of SPhPs by large frequency intervals on the PPLN and PPLT surfaces based on temperature adjustment. However, to couple these excitations to highly excited atoms, one must compare the spectral linewidths, ∼10 MHz, and the tuning ranges of the SPhPs to those of highly excited atoms, ∼10 kHz.

The tunability of the real SPhP resonance with superlattice constant variation is shown in Fig. 13 on both PPLN and PPLT surfaces. This plot is obtained by solving Eq. (30) for different superlattice constants. Our results show the SPhP's resonant frequency largely depends on the superlattice constant. Therefore, we can tune the SPhP resonance by constructing PSLs with different poling periods to design coupled Rydberg atom-SPhP systems.

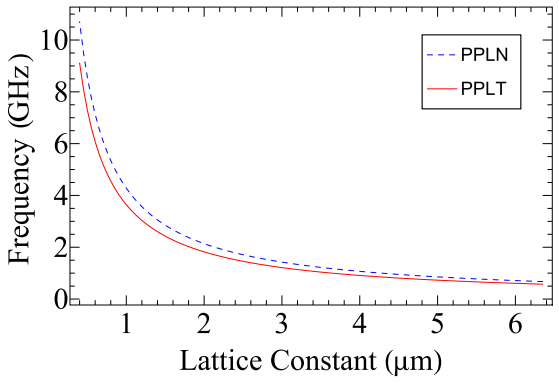

FIG. 13. The resonant frequencies of the real SPhP dispersion relation on T_yN_x surfaces at room temperature with respect to different artificial superlattice constants of PPLN (blue dashed curve) and PPLT (red solid curve) are shown. The superlattice constant l varies from 0.4 to 6.4 μm.

VI. SUMMARY

In this paper we calculated the dielectric response for specific PPLN and PPLT crystals and theoretically studied the SPhPs that exist at the interface between vacuum and a semi-infinite PSL. In the limit of small rotation of the PPLN and PPLT crystal dielectric principal axes away from the superlattice-surface orientation, the SPhP dispersion relations can be calculated analytically for TM-mode SPhPs with the SRA.

We did not consider the SPhP damping associated with the nonradiative loss to the crystal in this work. In addition to the intrinsic damping that exists on an ideal lossless crystal for pseudo-SPhPs, SPhPs decay nonradiatively by interacting with the material (phonon scattering, defect scattering, etc.) [47]. The nonradiative damping can be included in the elastic stiffness. The decay caused by coupling to the crystal depends on the temperature and the composition of the crystals [48,49]. The proper damping constants of lithium niobate and lithium tantalate are commonly chosen between $\gamma = 0.001\omega_m$ and $\gamma = 0.01\omega_m$ near each resonant frequency ω_m for theoretical studies [24,33,50]. For the calculation here, our real SPhP damping constant may be chosen approximately from 0.5 to 6 MHz. This can potentially be reduced by using thin samples suspended in space. The actual nonradiative damping can be obtained experimentally for specific crystals. In a real SPhP experiment on a finite-dimension PSL chip, where the the chip dimension is less than the size of the SPhPs, we would have to consider the interactions among the SPhPs on all sides of the chip surface. For the case of a thin metal or dielectric film, where the thickness of the film is less than the size of the supported surface polariton along the surface normal direction, the mixture of the two surface modes on opposite surfaces of the thin film has been studied [44,51,52]. The dispersion relation of a small dimension PSL chip is nontrivial to obtain with general boundary conditions on all sides of the chip surface.

By considering the piezoelectric effect, we calculated the dielectric response of the TM-mode electromagnetic field on a PSL. Based on the calculated dielectric response, within the

SRA, we determined the dispersion relations of SPhPs after considering the anisotropic nature of the superlattices. The SRA neglects a small intrinsic damping as the SPhP propagates along the PPLN and PPLT surfaces. Two types of polaritons, real SPhPs and virtual SPhPs, were shown to exist on the surfaces for six different superlattice-surface orientations. The real SPhPs can be supported on the T_yN_x surfaces for both PPLN and PPLT. The dispersion curves of the virtual SPhPs are similar to the real ones, but have a finite limit on the SPhP wave numbers. The real SPhPs and some of the virtual SPhPs are pseudosurface polaritons, but the intrinsic SPhP damping is small. Surface guided "almost photonlike" virtual SPhPs exist on the T_yN_x PPLN surface. All these SPhPs can be driven by infrared photons, the radiation of highly excited atoms, in the near field. Hence, the coupling of Rydberg transitions to the SPhPs on a PSL surface connects the atom-optical system to a solid state system and forms a quantum hybrid system [18]. The large tunability of the resonant frequencies on PSL surfaces provides flexibility for designing hybrid quantum systems, particularly in the area of optomechanics.

ACKNOWLEDGMENTS

This work was supported by NSF (PHY-1104424), AFOSR (FA9550-12-1-0282 and FA9550-15-5-0381), and the DARPA Quasar program by a grant through ARO (60181-PH-DRP). We thank Xi-kui Wu and Yan-qing Lu for useful discussions.

[1] W. L. Barnes, A. Dereux, and T. W. Ebbesen, Nature (London) **424**, 824 (2003).
[2] P. Berini and I. De Leon, Nat. Photon. **6**, 16 (2012).
[3] S. I. Bozhevolnyi, I. I. Smolyaninov, and A. V. Zayats, Phys. Rev. B **51**, 17916 (1995).
[4] P. Andrew and W. Barnes, Science **306**, 1002 (2004).
[5] S. V. Boriskina, J. K. Tong, Y. Huang, J. Zhou, V. Chiloyan, and G. Chen, *Photonics* (Multidisciplinary Digital Publishing Institute, Basel, Switzerland, 2015), Vol. 2, p. 659.
[6] A. González-Tudela, P. A. Huidobro, L. Martín-Moreno, C. Tejedor, and F. J. García-Vidal, Phys. Rev. Lett. **110**, 126801 (2013).
[7] J. P. B. Mueller and F. Capasso, Phys. Rev. B **88**, 121410 (2013).
[8] P. Törmä and W. L. Barnes, Rep. Prog. Phys. **78**, 013901 (2015).
[9] J. Zhang, L. Zhang, and W. Xu, J. Phys. D: Appl. Phys. **45**, 113001 (2012).
[10] A. Huber, N. Ocelic, D. Kazantsev, and R. Hillenbrand, Appl. Phys. Lett. **87**, 081103 (2005).
[11] N. Ocelic and R. Hillenbrand, Nat. Mater. **3**, 606 (2004).
[12] B. G. Ghamsari, X. G. Xu, L. Gilburd, G. C. Walker, and P. Berini, J. Opt. **16**, 114008 (2014).
[13] J. D. Caldwell, L. Lindsay, V. Giannini, I. Vurgaftman, T. L. Reinecke, S. A. Maier, and O. J. Glembocki, Nanophotonics **4**, 44 (2015).
[14] A. J. Huber, B. Deutsch, L. Novotny, and R. Hillenbrand, Appl. Phys. Lett. **92**, 203104 (2008).
[15] D. A. Chen, A. Narayanaswamy, and G. Chen, Phys. Rev. B **72**, 155435 (2005).
[16] S. Shen, A. Narayanaswamy, and G. Chen, Nano Lett. **9**, 2909 (2009).
[17] Y. Ming, Z. Wu, A. Tan, X. Hu, F. Xu, and Y. Lu, AIP Adv. **3**, 042122 (2013).
[18] H. Kübler, D. Booth, J. Sedlacek, P. Zabawa, and J. P. Shaffer, Phys. Rev. A **88**, 043810 (2013).
[19] L. Merten and G. Borstel, J. Raman Spectrosc. **10**, 205 (1981).
[20] E. Schuller, G. Borstel, and H. J. Falge, Phys. Status Solidi B **69**, 467 (1975).
[21] S. Lee, S. Ng, N. Al-Hardan, M. Abdullah, Z. Hassan, and H. A. Hassan, Thin Solid Films **519**, 3703 (2011).
[22] L. Airoldi, M. Senesi, and M. Ruzzene, in *Wave Propagation in Linear and Nonlinear Periodic Media*, CISM Courses and Lectures, Vol. 540, edited by F. Romeo and M. Ruzzene (Springer, Vienna, 2012), pp. 33–108.
[23] Y. Y. Zhu, X. J. Zhang, Y. Q. Lu, Y. F. Chen, S. N. Zhu, and N. B. Ming, Phys. Rev. Lett. **90**, 053903 (2003).
[24] Y. Q. Lu, Y. Y. Zhu, Y. F. Chen, S. N. Zhu, N. B. Ming, and Y. J. Feng, Science **284**, 1822 (1999).
[25] K. Huang, Proc. R. Soc. London Ser. A **208**, 352 (1951).
[26] C. Huang and Y. Zhu, AIP Adv. **2**, 042117 (2012).
[27] G. Borstel and H. J. Falge, Phys. Status Solidi B **83**, 11 (1977).
[28] K. Nakamura, H. Ando, and H. Shimizu, in *Proceedings of the IEEE 1986 Ultrasonics Symposium* (IEEE, 1986), p. 719.
[29] B. Auld, *Acoustic Fields and Waves in Solids* (Krieger, Malabar, FL, 1990), Vol. 1.
[30] Y. Y. Zhu, S. N. Zhu, Y. Q. Qin, and N. B. Ming, J. Appl. Phys. **79**, 2221 (1996).
[31] X. K. Hu, Y. Ming, X. J. Zhang, Y. Q. Lu, and Y. Y. Zhu, Appl. Phys. Lett. **101**, 151109 (2012).
[32] X. Zhang, D. Wu, C. Sun, and X. Zhang, Phys. Rev. B **76**, 085318 (2007).
[33] R. Yin, C. He, M. Lu, Y. Lu, and Y. Chen, J. Appl. Phys. **109**, 064110 (2011).
[34] R. F. Wallis, J. J. Brion, E. Burstein, and A. Hartstein, Phys. Rev. B **9**, 3424 (1974).
[35] R. T. Smith, Appl. Phys. Lett. **11**, 146 (1967).
[36] R. S. Weis and T. K. Gaylord, Appl. Phys. A **37**, 191 (1985).
[37] Y. Z. Wang, F. M. Li, W. H. Huang, X. Jiang, Y. S. Wang, and K. Kishimoto, Int. J. Solids Struct. **45**, 4203 (2008).
[38] B. Jaffe, W. Cook, and H. Jaffe, *Piezoelectric Ceramics, Non-metallic Solids* (Academic, New York, 1971).
[39] R. Warmbier, G. S. Manyali, and A. Quandt, Phys. Rev. B **85**, 085442 (2012).
[40] A. Hartstein, E. Burstein, J. Brion, and R. Wallis, Surf. Sci. **34**, 81 (1973).
[41] A. Hartstein, E. Burstein, J. Brion, and R. Wallis, Solid State Commun. **12**, 1083 (1973).
[42] L. Keldysh, A. Maradudin, and D. Kirzhnitz, *The Dielectric Function of Condensed Systems*, Modern Problems in Condensed Matter Sciences (Elsevier, Amsterdam, 2012).

[43] E. Lim, *Excited States* (Elsevier Science, Amsterdam, 2013), Vol. 6.
[44] D. MIRLIN, in *Surface Polaritons Electromagnetic Waves at Surfaces and Interfaces*, Modern Problems in Condensed Matter Sciences, Vol. 1, edited by V. Agranovich and D. Mills (Elsevier, Amsterdam, 1982), pp. 3–67.
[45] R. T. Smith and F. S. Welsh, J. Appl. Phys. **42**, 2219 (1971).
[46] Y. S. Kim and R. T. Smith, J. Appl. Phys. **40**, 4637 (1969).
[47] U. T. Schwarz and M. Maier, Phys. Rev. B **58**, 766 (1998).
[48] S. Kojima, Jpn. J. Appl. Phys. **32**, 4373 (1993).
[49] B. Bittner, M. Scherm, T. Schoedl, T. Tyroller, U. T. Schwarz, and M. Maier, J. Phys. Condens. Matter **14**, 9013 (2002).
[50] X. J. Zhang, R. Q. Zhu, J. Zhao, Y. F. Chen, and Y. Y. Zhu, Phys. Rev. B **69**, 085118 (2004).
[51] A. V. Zayats, I. I. Smolyaninov, and A. A. Maradudin, Phys. Rep. **408**, 131 (2005).
[52] L. Wendler and R. Haupt, J. Phys. C: Solid State Phys. **19**, 1871 (1986).